Soft Matter

www.rsc.org/softmatter

Volume 9 | Number 9 | 5 March 2013 | Pages 2543–2770

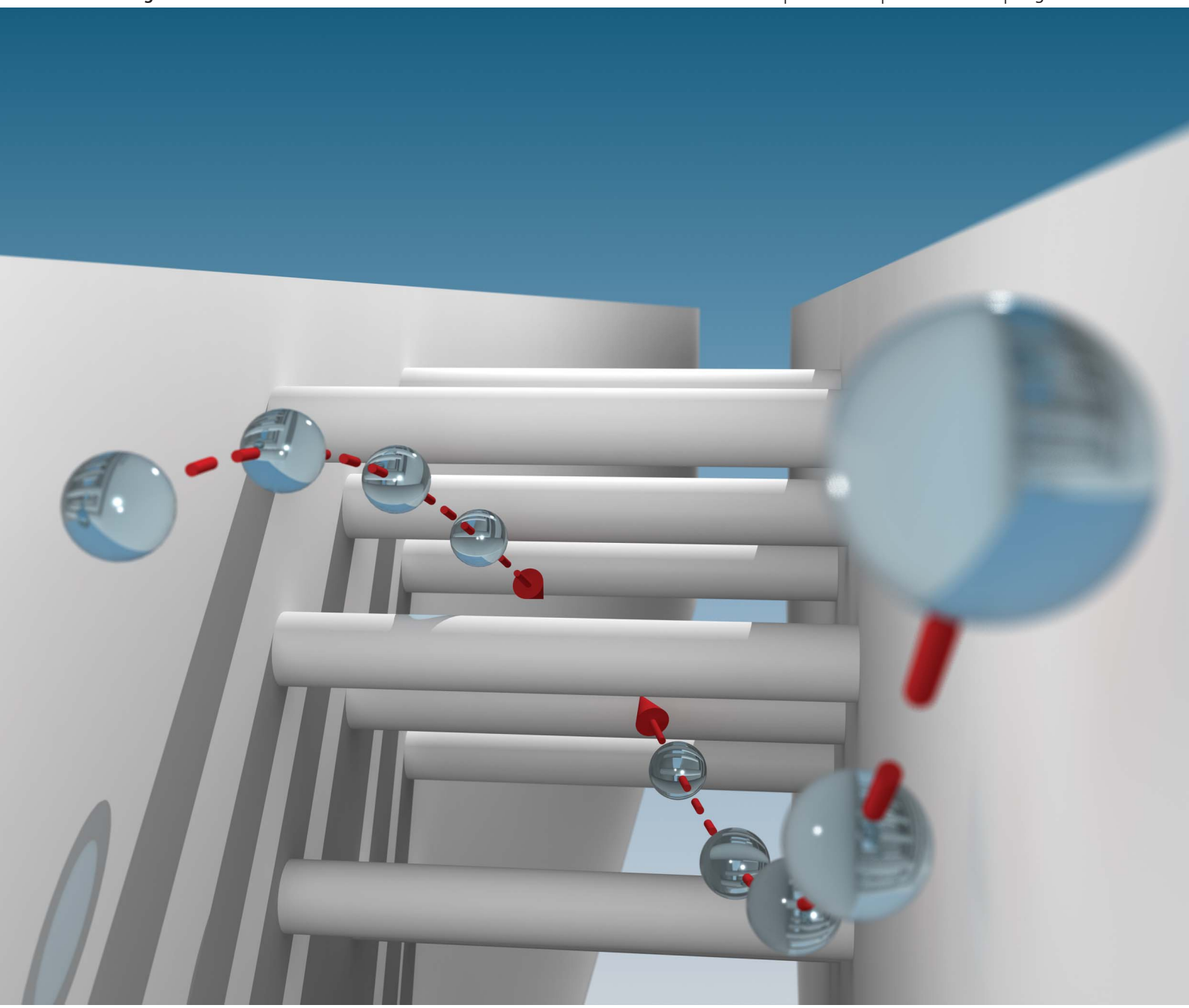

ISSN 1744-683X

RSC Publishing

PAPER

Arash Nikoubashman *et al.*

Computer simulations of colloidal particles under flow in microfluidic channels

1744-683X(2013)9:9;1-C

Soft Matter

RSC Publishing

PAPER

Computer simulations of colloidal particles under flow in microfluidic channels

Cite this: *Soft Matter*, 2013, **9**, 2603

Arash Nikoubashman,*[ab] Christos N. Likos[c] and Gerhard Kahl[a]

We study the propagation of single, neutrally buoyant rigid spheres under pressure-driven flow by means of extensive computer simulations that correctly account for hydrodynamic interactions. We first consider a system geometry consisting of two parallel plane walls and achieve very good agreement with experimental results [M. E. Staben and R. H. Davis, *Int. J. Multiphase Flow*, 2005, **31**, 529]. In the second part of our analysis, we simulate the flow of tracer particles through a hexagonal array of cylindrical obstacles, whose axis lies parallel to the gradient–vorticity plane of the flow. We find that the presence of the obstacles causes a significant slowdown of the tracer particles and that their velocities respond in a highly non-linear way to an increasing pressure drop.

Received 26th July 2012
Accepted 19th December 2012

DOI: 10.1039/c2sm26727f

www.rsc.org/softmatter

Published on 17 January 2013 on http://pubs.rsc.org | doi:10.1039/C2SM26727F
Downloaded by Princeton University on 07 February 2013

I Introduction

Particle transport in narrow channels is a problem of high relevance in many biological and industrial processes, such as blood flow,[1] suspension flow[2,3] and separation of size-dispersed colloids at the micro- and nano-scale.[4] With the advent of novel microfluidic devices, featuring cross-sectional dimensions on the order of tens to hundreds of microns and lengths of centimeters, these systems have become much more accessible to experiments.[5,6] So far, a considerable amount of research has been carried out for a variety of systems, ranging from DNA analysis[7–9] and microchip-based polymer electrophoresis[10–12] over heat management[13] to display technology.[14]

Despite the aforementioned advances, the fundamental problem of how a *single* rigid sphere behaves under pressure driven flow has only been studied recently by Staben and Davis, where they have conducted systematic particle-tracking experiments for a wide range of tracer sizes.[15] One challenging aspect of such experiments is that the tracer size can become comparable to the channel diameter, rendering both the response of the solvent and the particle–wall interactions very important. In addition, the construction of microfluidic devices has often focused on ease of fabrication without much consideration for the entrance geometry of the microchannel, which can lead to non-optimal distribution of particles in the microchannels.

From the theoretical point of view, this particular problem has its roots in the related issue of how a spherical particle propagates in the vicinity of a single wall.[16] This problem was then eventually extended by Faxén to the case of two planar walls,[17] but under the rather strict limitation that the particle is placed on the centerline or at one-fourth of the distance between the two walls. Ganatos *et al.* have worked towards a more general answer to this question by decomposing the problem into four parts:[18,19] translation of a sphere without rotation, rotation of a sphere without translation, and Poiseuille and shear flow past a pinned sphere. For small Reynolds numbers, Re, *i.e.* when the dynamics of the system is governed by viscous forces as opposed to inertia, these individual contributions can then be linearly summed up again to find the final solution. This approximation however only provides an accurate description for the flow behavior of rigid particles whose surface has a distance of at least 10% of their radius from either wall.

In more recent works, numerically more demanding techniques, such as the Arbitrary Lagrangian–Eulerian method[20] and boundary-integral (BI) algorithms,[21] have been employed successfully to predict the flow behavior close to the channel walls. However, these techniques are not suitable to study more complicated systems that involve, for instance, multiple tracer particles or fixed obstacles. Ghosh *et al.* have studied such a confined system by means of Brownian dynamics simulation, where an overdamped, two-dimensional particle has been driven through a rectangular array of circular obstacles.[22] Despite the two-dimensional nature of their simulations and the lack of hydrodynamic interactions (HI), they have captured essential properties of such confined systems, such as negative differential mobilities and unconventional asymptotic behaviors.

In this work, we first consider a slab-like channel consisting of two parallel planar walls, and study the motion of a single, neutrally buoyant colloidal particle under Poiseuille flow at low-Reynolds number conditions. To this end, we carried out

[a]*Institute of Theoretical Physics and CMS, Vienna University of Technology, Wiedner Hauptstraße 8-10, A-1040 Vienna, Austria. E-mail: arashn@princeton.edu*

[b]*Department of Chemical and Biological Engineering, Princeton University, Princeton, New Jersey 08544, USA*

[c]*Faculty of Physics, University of Vienna, Boltzmanngasse 5, A-1090 Vienna, Austria*

Published on 17 January 2013 on http://pubs.rsc.org | doi:10.1039/C2SM26727F
Downloaded by Princeton University on 07 February 2013

extensive computer experiments that correctly take hydrodynamic interactions into account. The employed simulation technique reproduces the experimental results for rigid spherical particles within the free channel remarkably well.[15]

There is a growing interest to study microfluidic systems at Reynolds-numbers well above unity in both experiments[23,24] and simulations.[25] Therefore, in the second part of our work, we analyze the motion of tracer particles through hexagonal micropost arrays at Re $\gtrsim$ 1.0. We establish that the presence of hindrances causes a significant slowdown of the colloidal particles, and that their velocities are not proportional to the applied pressure gradient anymore, but respond to it in a highly non-linear fashion. We provide a detailed explanation of this unusual behavior by considering the flow behavior around the stack of pillars.

The rest of this paper is organized as follows. In Section II we present our model and simulation method. Our results concerning the planar walls are presented and discussed in Section III, and the ones pertaining to the transport flow in confinement in Section IV. Finally, we summarize our findings and draw our conclusions in Section V.

II Simulation method

In order to incorporate HI as faithfully as computationally feasible, we have opted to employ a hybrid simulation approach, in which standard molecular dynamics (MD) algorithms are combined with the Multi-Particle Collision Dynamics (MPCD) simulation technique.[26,27] This choice is motivated by the large disparities in the length and time scales, characteristic for the solvent molecules and the embedded particles, which make atomistic simulation studies prohibitively time-consuming. This simulation scheme has already been successfully employed for similar problems in capillary flow,[28–31] and we will present a detailed description of the method in what follows.

MPCD is a mesoscopic, particle-based simulation method, consisting of alternating *streaming* and *collision* steps, where the solvent particles are assumed to be non-interacting. The coupling between the solvent and solute particles is realized through momentum exchange. In what follows, we will denote the properties of the solvent particles with lowercase letters and the ones of the solute particles with uppercase ones. During the streaming step, the solvent particles of unit mass m propagate ballistically over a period of Δt:

$$\boldsymbol{r}_i(t + \Delta t) = \boldsymbol{r}_i(t) + \Delta t \boldsymbol{v}_i(t), \tag{1}$$

where $\boldsymbol{r}_i(t)$ is the position and $\boldsymbol{v}_i(t)$ the velocity of i-th solvent particle at time t. In the collision step, the solvent particles are first grouped into collision cells and then undergo stochastic collisions with particles within the same cell, updating thus their velocities $\boldsymbol{v}_i(t)$ into their new values $\boldsymbol{v}_i(t + \Delta t)$ as:

$$\boldsymbol{v}_i(t + \Delta t) = \boldsymbol{u}_j(t) + \Omega(\alpha)[\boldsymbol{v}_i(t) - \boldsymbol{u}_j(t)]. \tag{2}$$

Here, $\boldsymbol{u}_j$ denotes the center of mass velocity of the j-th collision cell, while $\Omega(\alpha)$ is a norm-conserving rotation matrix around a randomly chosen axis by some fixed angle α. Due to the cell-based nature of this algorithm, the spatial resolution of the HI is determined by the mesh size of the collision cells, a. The mean free path of a solvent particle is then given by $\lambda \sim \Delta t\sqrt{T}$, and it has been shown in ref. 32 that Galilean invariance is violated for $\lambda < a/2$. Therefore, all lattice cells are shifted by a randomly chosen vector, drawn from a cube with edge length in the interval $[-a/2, +a/2]$ before each collision step. While the above-described rules governing the solvent dynamics are general, the simulation of specific flow profiles requires special care and will be discussed in what follows.

Poiseuille flow is driven by a pressure gradient in the flow (z) direction, and is slowed down by viscous drag along both plates, so that these forces are in balance. The walls are separated by a distance L_x along the gradient (x) direction. Additionally, we have applied no-slip boundary conditions for the solvent particles with the walls along this direction, and periodic boundary conditions in the vorticity (y) and flow direction for both the solvent and the solute. The geometry of this setup and the flow pattern generated for the pure solvent are schematically illustrated in Fig. 1. From the computational point of view, several methods exist for generating such a flow, for instance forced,[26,33,34] surface-induced, and gravitational[31,35] approaches. In our simulations, we adopted the latter technique, since the other two methods lead to a considerable distortion of the velocity-field and density profile along the flow direction.[35] In this case, the external force acting on the unit volume of the fluid, $\mathscr{F}$, is given by $\mathscr{F} = \varrho_s g\hat{z}$, where ϱ_s is the mass density of the solvent, g is the acceleration constant and $\hat{z}$ is the unit vector in the flow direction. The effect of $\mathscr{F}$ can easily be incorporated into the streaming step as follows:

$$\boldsymbol{r}_i(t + \Delta t) = \boldsymbol{r}_i(t) + \Delta t \boldsymbol{v}_i(t) + \frac{\Delta t^2}{2} g\hat{z}; \tag{3}$$

$$\boldsymbol{v}_i(t + \Delta t) = \boldsymbol{v}_i(t) + \Delta t g\hat{z}. \tag{4}$$

The strength of the gravitational field can be varied by tuning g, and a steady Poiseuille flow builds up self-consistently after a short time when no-slip boundary conditions are applied at the surface layers. For planar walls coinciding with the collision cell boundaries, such conditions are conveniently implemented by employing a bounce-back rule, *i.e.*, the velocities of particles that hit the walls are inverted after the collision.

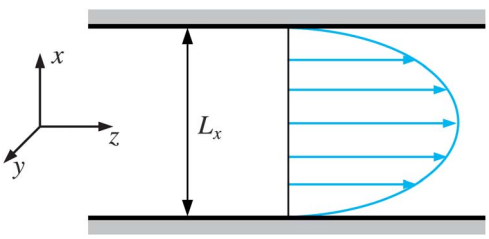

Fig. 1 Schematic representation of the simulation setup for Poiseuille flow, demonstrating the flow (z), gradient (x), and vorticity (y) directions, and the resulting velocity profile for the pure solvent.

 This journal is © The Royal Society of Chemistry 2013

Published on 17 January 2013 on http://pubs.rsc.org | doi:10.1039/C2SM26727F
Downloaded by Princeton University on 07 February 2013

However, for a more general system geometry the walls will not coincide with, or will not even be parallel to the collision cell boundaries. Furthermore, partially occupied collision cells can also emerge from the cell-shifting, which is unavoidable for small mean free paths λ. Lamura *et al.* have demonstrated that in such a case the bounce-back rule has to be modified by refilling of boundary cells with virtual particles.[34,36] This feature has been included in our implementation for all intersected cells, including those cells which contained segments of the cylindrical obstacles (see Section IV). Additionally, thermostatting is required in any non-equilibrium MPCD simulation whenever either isothermal conditions are required or viscous heating can occur. The thermostat employed was based on rescaling the velocities at the cellular level to maintain constant temperature.[31]

Furthermore, we modeled the interaction between the solute particles and the walls by a soft repulsive potential of the form:[37]

$$U_{\mathrm{W}}(x) = \begin{cases} \frac{2}{3}\pi\varepsilon_{\mathrm{W}}\left[\frac{2}{15}\left(\frac{\sigma}{x}\right)^{9} - \left(\frac{\sigma}{x}\right)^{3} + \frac{\sqrt{10}}{3}\right], & 0 \le x \le (2/5)^{1/6}\sigma \\ 0, & x > (2/5)^{1/6}\sigma. \end{cases} \quad (5)$$

In the equation above, x denotes the distance between the wall and the center of the solute particle, whose diameter is given by σ. The strength of the potential can be tuned *via* the parameter ε_{W}, and we chose a value of $\varepsilon_{\mathrm{W}} = 0.05k_{\mathrm{B}}T$ in our simulations. The total external potential caused by both walls is then given by the superposition $U_{\mathrm{ext}}(x) = U_{\mathrm{wall}}(x) + U_{\mathrm{wall}}(L_x - x)$.

The MPCD parameters employed were $\alpha = 130^{\circ}$ and $\lambda = 0.1a$, with 10 solvent particles per collision cell, and all simulations were run at $T = 1$. For the conventional MD-timestep, we employed a Verlet integration scheme with $\Delta t_{\mathrm{MD}} = 2 \times 10^{-3}$, whereas the MPCD time step was $\Delta t = 10^{-1}$, both measured in the unit of time $\tau = \sqrt{ma^2/(k_{\mathrm{B}}T)}$. The unit of the acceleration constant g is then given by a/τ^2. For these simulation parameters, the dynamic viscosity of the solvent reads $\eta = 8.5\tau k_{\mathrm{B}}T/a^3$. For experiments conducted at room temperature and channel diameters of a few μm, the employed parameters describe an aqueous solvent with $\eta \sim 10^{-4}$ Pa·s.

A Coupling between solvent and solute particles

In MPCD simulations, many different approaches exist for coupling a suspended solute particle to the surrounding solvent, and for an extensive overview we refer the reader to ref. 27 and 38. A commonly used method is to sort the solute particles into the collision cells, and include their velocities in the rotation step.[39] Although this approach seems oversimplified at first glance, it has been shown in ref. 40 that the dynamics of the solute particles (polymer chains in this particular case) are correctly reproduced when the associated monomers are coupled to the solvent in this way. This technique has been employed for the simulation of, amongst others, star polymers,[41] dendrimers,[31] and claylike colloids.[28,29] However, the disadvantage of this method is that only the solvent particles within the same cell are taken into account for the coupling. Thus, the flow field around the colloidal particle cannot be resolved in detail: neither the fact that colloidal particles push away the solvent nor depletion and lubrication forces can be reproduced at any level.

Another possibility is to couple the solvent and solute particles through repulsive central forces.[33] However, such a force has to be rather strong to prohibit the solvent particles from penetrating the colloids. Therefore, when implementing this procedure, a sufficiently small time step Δt is required in order to resolve these interactions correctly, and a large number of MD time steps are needed during the streaming step. An additional drawback of this approach is that only slip boundary conditions can be modeled with central forces. This deficiency can be easily understood on the basis of the following example: first, assume a buoyant colloidal particle surrounded by resting solvent particles; then spin the colloid without moving it from its original position. If the solvent particles are coupled to the colloid only by a central force, they will not react to this rotation, since the mutual distances remain unchanged during this process. In reality however, the surface of a colloid is never perfectly smooth, and therefore the solvent close to the colloid will be dragged along. The detailed molecular origins of these boundary conditions are subtle problems, and for a recent review of the extensive literature on this subject, see ref. 42.

In this work, we pursue a different route, following the arguments put forward by Inoue *et al.*,[43] and couple the solute to the solvent particles through the exchange of both *linear* and *angular* momenta during the streaming step. First we check after each streaming step whether the new position of the i-th solvent particle lies within a colloidal particle. If this is the case, we stochastically deflect the solvent particle from the colloid and transfer the momentum to the colloid. In what follows, we will discuss this procedure in more detail.

Fig. 2(a) depicts the collision process between a point-like solvent particle and an impenetrable colloid, located at $\boldsymbol{R}_j(t)$. At initial time t, the solvent particle is located at $\boldsymbol{r}_i(t)$ and propagates ballistically over a timestep Δt with velocity $\boldsymbol{v}_i(t)$. Along its trajectory, it crosses the surface of the colloid at the point $\boldsymbol{r}^*$. In order to calculate the exact time and location of the collision, we first write down the equation of a sphere, centered at $\boldsymbol{R}_j$:

$$\left|\boldsymbol{r} - \boldsymbol{R}_j\right|^2 = \frac{\sigma^2}{4}, \quad (6)$$

and of a linear trajectory in space, originating at $\boldsymbol{r}_i$:

$$\boldsymbol{r} = \boldsymbol{r}_i + \Delta x \hat{\boldsymbol{v}}_i. \quad (7)$$

here, Δx denotes the distance covered within Δt, and $\hat{\boldsymbol{v}}_i$ is the normalized velocity of the solvent particle. We can then determine the exact location of impact, $\boldsymbol{r}^* = \boldsymbol{r}_i + \Delta x^* \hat{\boldsymbol{v}}_i$, by solving eqn (6) and (7) for Δx:

$$\Delta x^*_{1,2} = -\left(\boldsymbol{r}_i \cdot \hat{\boldsymbol{v}}_i - \boldsymbol{R}_j \cdot \hat{\boldsymbol{v}}_i\right) \pm \sqrt{\left(\boldsymbol{r}_i \cdot \hat{\boldsymbol{v}}_i - \boldsymbol{R}_j \cdot \hat{\boldsymbol{v}}_i\right)^2 - \boldsymbol{r}_i^2 - \boldsymbol{R}_j^2 + 2\boldsymbol{r}_i \cdot \boldsymbol{R}_j + \sigma^2/4}, \quad (8)$$

and inserting the smaller value of the resulting Δx^*'s back in eqn (7). However, this procedure is computationally quite

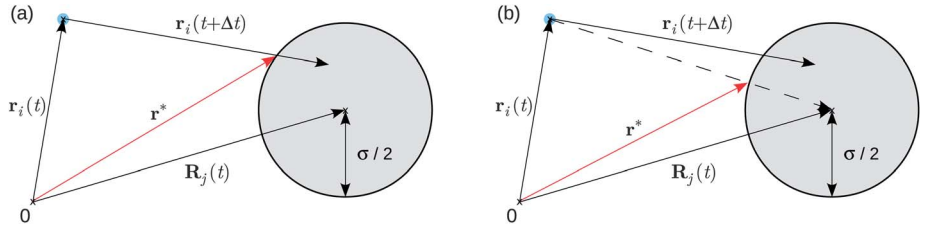

Fig. 2 Schematic representation of the exact (a) and approximate (b) collision process between a solvent particle with index *i* and an impenetrable colloid *j* with diameter σ. The vector $\boldsymbol{r}_i(t)$ denotes the position of the solvent particle at time *t*, while $\boldsymbol{R}_j(t)$ denotes the position of the colloid. The vector $\boldsymbol{r}^*$ (red arrow) indicates the point of impact in the case of the exact and approximate calculation (see text).

Published on 17 January 2013 on http://pubs.rsc.org | doi:10.1039/C2SM26727F
Downloaded by Princeton University on 07 February 2013

expensive, and it has been shown in ref. 28 and 44 that such a detailed description is not necessary. Instead, it is sufficient to estimate the point of impact by the closest point on the surface of the colloidal particle. This approximation is schematically shown in Fig. 2(b), and $\boldsymbol{r}^*$ is then simply given by:

$$\boldsymbol{r}^* = \boldsymbol{R}_j + \frac{\sigma}{2}\frac{\boldsymbol{r}_i - \boldsymbol{R}_j}{|\boldsymbol{r}_i - \boldsymbol{R}_j|} = \boldsymbol{R}_j + \frac{\sigma}{2}\hat{e}_n. \tag{9}$$

Then, we move the solvent particle with its reflected velocity for half of a time step. In order to implement the momentum exchange between the solvent and the solute, one could try to apply the same extended bounce-back collision rule that we incorporated for the planar walls. However, Padding *et al.* have demonstrated that these boundary conditions result in rotational frictions that turned out to be larger than expected.[44] This deficiency presumably stems from the fact that the colloidal particles can move and therefore have a local temperature, in contrast to the immobile walls considered in the preceding subsection.

Alternatively, the solvent particles can be scattered from the colloidal target in a stochastic way, where upon collision, the particles are assigned random normal and tangential velocities v_n^* and v_t^* respectively (relative to the velocity of the colloid). For sufficiently small mean free paths, $\lambda \ll \sigma$, the probability distribution for the scattered velocity is given by:[28,43,44]

$$p(v_n^*) = m\beta v_n^* \exp(-m\beta v_n^{*2}/2), \tag{10}$$

$$p(v_t^*) = \sqrt{m\beta/(2\pi)}\exp(-m\beta v_t^{*2}/2), \tag{11}$$

with inverse temperature β. Then after the collision, the final velocities of the solvent particle *i* and the colloid *j* read:

$$\boldsymbol{v}_i(t+\Delta t) = \boldsymbol{V}_j(t) + \boldsymbol{L}_j(t)\times[\boldsymbol{r}^* - \boldsymbol{R}_j(t)] + v_n^*\hat{e}_n + v_t^*\hat{e}_t, \tag{12}$$

$$\boldsymbol{V}_j(t+\Delta t) = \boldsymbol{V}_j(t) + \frac{m}{M}\left[\boldsymbol{v}_i(t) - \boldsymbol{v}_i(t+\Delta t)\right], \tag{13}$$

with the normal and tangential unit vectors $\hat{e}_n$ and $\hat{e}_t$, and the colloid's mass *M*. As a result of the additional tangential component of the velocity that the colloidal particle acquires, its angular velocity $\boldsymbol{L}_j(t)$ is modified as well, and after the collision it has a value given by:

$$\boldsymbol{L}_j(t+\Delta t) = \boldsymbol{L}_j(t) + \frac{m}{I}\left[\boldsymbol{r}^* - \boldsymbol{R}_j(t)\right]\times\left[\boldsymbol{v}_i(t) - \boldsymbol{v}_i(t+\Delta t)\right], \tag{14}$$

with the moment of inertia $I = M\sigma^2/10$.

III Propagation of a single particle through a channel

In the first part of our investigations, we analyzed the translational motion of a single colloidal particle in the presence of pressure driven flow by employing the simulation approach described above. In such a scenario, the Reynolds number is given by:

$$\mathrm{Re} = \frac{\sigma v_0}{\eta/\varrho_s}. \tag{15}$$

here, v_0 denotes the maximum velocity of the solvent (see further below), and we conducted our simulations at $\mathrm{Re} \lesssim 1.0$. We used a rectangular channel of size $V = (40 \times 80 \times 160)a^3$, with a total of 512×10^4 solvent particles. Here, we deliberately chose the extent of the channel to be comparatively large in the vorticity (L_y) and in the flow direction (L_z), in order to minimize finite size effects. Furthermore, lateral motions of the solute particle along the gradient direction were inhibited by imposing a harmonic potential:

$$U_H(x) = 20k_BT(x - x_0)^2, \tag{16}$$

which restricts the particle's displacement *x* along the gradient direction to be close to the designated position x_0.

Poiseuille flow, enclosed by two parallel plates positioned at $x = 0$ and $x = L_x$, is driven by a pressure gradient parallel to the flow direction, and is slowed down by viscous drag along both plates, so that the resulting forces are in balance. Under such conditions, a parabolic velocity profile builds up:

$$v_z(x) = \frac{\varrho_s g}{2\eta}(L_x - x)x. \tag{17}$$

In eqn (17) above, the solvent viscosity η is determined by the solvent mass density ϱ_s and the collision rules, *i.e.*, it is *not* an input parameter to the simulation (see Section II). The velocity profile vanishes at $x = 0$ and at $x = L_x$, and attains its maximum value, v_0, at the middle of the channel ($x = L_x/2$), *viz.*:

$$v_0 = \frac{\varrho_s g L_x^2}{8\eta}. \tag{18}$$

For dispersed solute particles, the spatial velocity distribution is not readily available, since their flow behavior strongly depends on, *e.g.*, their concentration, shape and size. Additionally, the presence of the solute also affects the shape of the

 This journal is © The Royal Society of Chemistry 2013

Published on 17 January 2013 on http://pubs.rsc.org | doi:10.1039/C2SM26727F
Downloaded by Princeton University on 07 February 2013

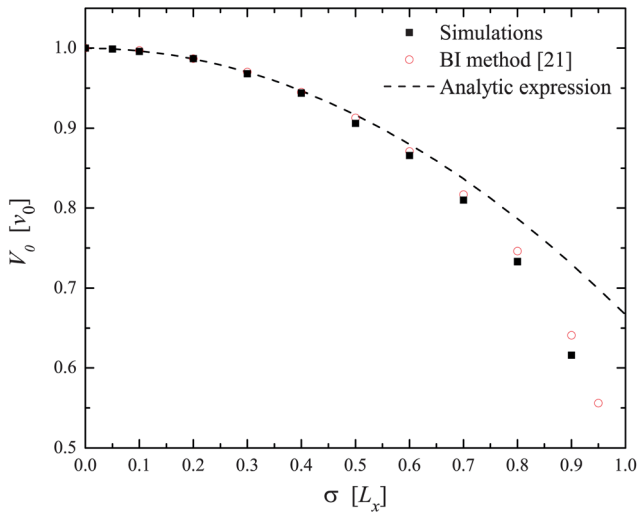

Fig. 3 Translational velocity V_0 of a centrally placed solute particle as a function of its diameter σ in a channel of width L_x. Black symbols show results from our MPCD simulations, while the red open symbols display the results from ref. 21 obtained with the BI method. The dashed line represents the results from eqn (20).

flow profile, rendering the problem even more complex. For very small dispersed particles ($\sigma \ll L_x$) and at low solute concentrations, however, the geometric details of the solute can be ignored and the velocity profile of the surrounding fluid can safely be regarded as unperturbed. Under such conditions, the simplest way to derive the average translational velocity of a dispersed particle is to integrate over the given velocity profile $v_z(x)$ across the extension of the particle in the x-direction:

$$V_z(x) = \frac{1}{\sigma}\int_{x-\sigma/2}^{x+\sigma/2} v_z(x')\mathrm{d}x' = \frac{\varrho_s g}{2\eta}\left[L_x x - x^2 - \frac{1}{3}\left(\frac{\sigma}{2}\right)^2\right], \qquad (19)$$

where x denotes the distance of the particle's center to the lower channel wall. If we place the solute exactly in the middle of the channel ($x = L_x/2$), denote $V_0 \equiv V_z(L_x/2)$, and normalize eqn (19) by the unperturbed centerline velocity, v_0, then we get:

$$\frac{V_0}{v_0} = 1 - \frac{1}{3}\frac{\sigma^2}{{L_x}^2}. \qquad (20)$$

Strictly speaking, eqn (19) is unphysical, since different parts of a rigid particle cannot move with different velocities. Instead, the integration has the meaning that the resulting velocity $V_z(x)$ is the velocity with which the particle center is moving. Thus, the parabolic profile of eqn (17) is not smooth anymore, but rather a series of steps of width σ. In Fig. 3, we compare the analytic expression of a dispersed particle, given in eqn (20), with our simulation data for the case that the particle has been placed in the center of the channel. In this region, the curvature of the velocity profile vanishes, and we observe that the motion of small solute particles ($\sigma \lesssim 0.3L_x$) is well predicted by eqn (20). However, this picture eventually breaks down with increasing particle diameter. In addition to the aforementioned deficiencies, a further reason for the failure of eqn (19) at large σ is the lack of any hydrodynamic coupling between the solute and the solvent in this description; it is clearly visible from Fig. 3 that this approximation leads to an overestimation of the solute velocities, since the analytic result for V_0 is systematically larger than the values obtained from the simulations.

Table 1 Dimensionless translational velocities $V_z(x)/v_0$ of a spherical dispersed particle for various diameters σ. The first row contains the studied diameters σ, while the first column shows the inspected wall distances x, beginning with the central placement $L_x/2$. Empty cells correspond to positions beyond the centerline $L_x/2$, while cells containing dashes ("—") represent unphysical configurations, where the solute particle would extend into the system's walls. The measurement uncertainty of the presented values lies within 3%

	σ/L_x									
x	0.05	0.1	0.2	0.3	0.4	0.5	0.6	0.7	0.8	0.9
$L_x/2$	0.999	0.996	0.987	0.968	0.944	0.906	0.866	0.810	0.733	0.616
7.0σ	0.914		—	—	—	—	—	—	—	—
4.0σ	0.646	0.956		—	—	—	—	—	—	—
3.0σ	0.515	0.841		—	—	—	—	—	—	—
2.0σ	0.365	0.642	0.955			—	—	—	—	—
1.6σ	0.299	0.542	0.860	0.959		—	—	—	—	—
1.4σ	0.265	0.488	0.799	0.932			—	—	—	—
1.2σ	0.230	0.427	0.721	0.877	0.939		—	—	—	—
1.0σ	0.195	0.366	0.629	0.791	0.890			—	—	—
0.9σ	0.176	0.332	0.579	0.739	0.843	0.893			—	—
0.8σ	0.156	0.296	0.525	0.681	0.781	0.851	0.862		—	—
0.7σ	0.137	0.262	0.466	0.613	0.700	0.776	0.821	0.807		—
0.6σ	0.118	0.224	0.390	0.533	0.596	0.656	0.710	0.750	0.729	
0.575σ	0.114	0.214	0.362	0.510	0.566	0.619	0.668	0.706	0.715	
0.56σ	0.112	0.206	0.349	0.493	0.545	0.591	0.639	0.675	0.694	
0.55σ	0.109	0.202	0.336	0.483	0.527	0.574	0.619	0.650	0.677	0.614
0.535σ	0.107	0.196	0.319	0.467	0.509	0.543	0.584	0.608	0.646	0.605
0.52σ	0.104	0.190	0.302	0.452	0.485	0.509	0.538	0.560	0.600	0.575
0.51σ	0.102	0.185	0.285	0.440	0.475	0.492	0.511	0.523	0.556	0.535
0.505σ	0.101	0.183	0.282	0.430	0.465	0.475	0.490	0.494	0.529	0.498

Published on 17 January 2013 on http://pubs.rsc.org | doi:10.1039/C2SM26727F
Downloaded by Princeton University on 07 February 2013

On a more quantitative level, Table 1 shows the simulation results for the dimensionless translational velocities $V_z(x)/v_0$ of a dispersed, spherical particle under Poiseuille flow. Here, we varied the particle's distance x to the wall and considered different values for the diameter σ of the dispersed particle. As expected, the retardation of the particle motion relative to the fluid motion is more sizable for larger particles and for particles closer to either of the walls; this effect is due to the curvature of the parabolic flow field and the stress exerted by the solvent on the solute in the narrow gap formed by its surface and the channel wall.

Fig. 4 shows the velocity distributions $V_z(x)$ for selected particle diameters. A distinct narrowing and slowing down with respect to $v_z(x)$ is visible, which becomes more pronounced as σ increases. This size-dependence can be traced back to the fact that larger particles have less space for lateral movement in the channel, and thus block the solvent flow much more severely than smaller tracer particles do.

Another quantity of interest is the mean particle velocity in the flow direction, $\langle V_z \rangle$, averaged over the channel width; this quantity is often more easily accessible in experiments than the spatially resolved velocity profile $V_z(x)$. In what follows, we will compare this value to the average velocity of the pure solvent, $\langle v_z \rangle = 2v_0/3$. Brenner and Gaydos have derived an asymptotic expression for the average particle velocity of a uniform suspension of small spherical particles under Poiseuille flow in a tube of circular cross-section,[45] and their calculation has been extended to the present rectangular geometry in ref. 21:

$$\langle V_z \rangle / \langle v_z \rangle = 1 + \sigma/L_x - 2.02(\sigma/L_x)^2 + \mathcal{O}[(\sigma/L_x)^3]. \qquad (21)$$

According to eqn (21), the average tracer velocity first increases with increasing particle diameter σ, and then reaches its maximum at $\sigma \approx 0.25L_x$. This effect is due to the exclusion from the slower-moving solvent particles within a distance of the radius of the tracer particle to either wall. With increasing σ, the trend reverses as retardation effects of the channel walls and the curved velocity profile on large particles become progressively dominant. $\langle V_z \rangle$ decreases monotonically until it eventually drops below the average velocity of the pure solvent, $\langle v_z \rangle$, at $\sigma \approx 0.5L_x$. The σ-dependence of $\langle V_z \rangle$ is shown in Fig. 5, which displays the results from the asymptotic theory, eqn (21), our simulation data, as well as the numerical and experimental findings from Staben *et al.* (ref. 15 and 21, respectively). From these data it is well visible that the asymptotic theory predicts the averaged velocity correctly for very small particles but considerably underestimates it for $\sigma \gtrsim 0.15L_x$. Compared to the analytic expression, eqn (21), the simulation data reach the aforementioned maximum for slightly larger particles ($\sigma \approx 0.30L_x$), and become equal to the average fluid velocity $\langle v_z \rangle$ for $\sigma \approx 0.82L_x$. We emphasize that our findings are in almost perfect quantitative agreement with previously established numerical[21] and experimental results,[15] confirming the validity of our approach. Thus, we can safely extend our method to more involved systems, containing, *e.g.*, one or multiple obstacles.

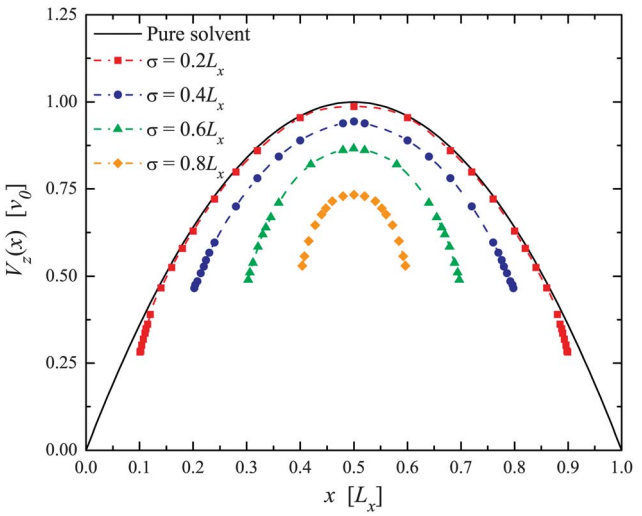

Fig. 4 Velocity distributions $V_z(x)$ for particle diameters $\sigma = 0.2L_x$ (red), $\sigma = 0.4L_x$ (blue), $\sigma = 0.6L_x$ (green) and $\sigma = 0.8L_x$ (orange). The velocity profile of the pure solvent (*i.e.* in the absence of solute particles) is indicated by the solid line (black) [*cf.* eqn (17)].

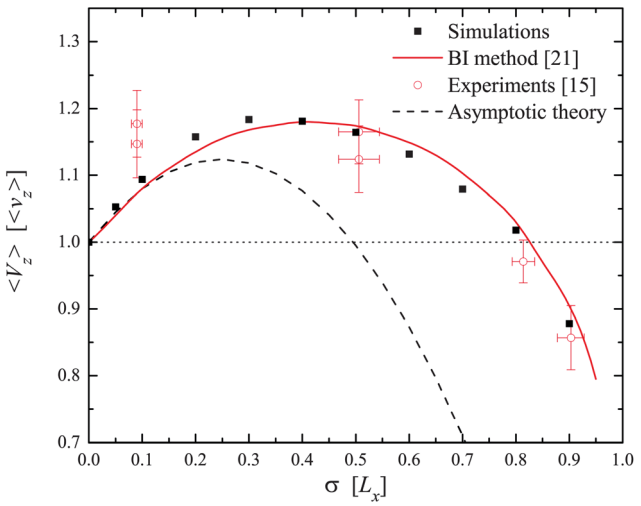

Fig. 5 Average particle velocity, $\langle V_z \rangle$, normalized to the average fluid velocity, $\langle v_z \rangle$, as a function of the particle diameter σ. Black symbols show results from our MPCD simulations, while the solid red curve shows the data of the BI calculations presented in ref. 21. The red open symbols show experimental results from ref. 15. The dashed curve represents the data from the asymptotic theory[21] [*cf.* eqn (21)].

IV Propagation of a particle through a porous environment

The flow of simple and complex liquids through porous media is ubiquitous in our daily lives, and a better understanding of this process bears great importance in both fundamental and applied science.[46,47] For instance, the flow through highly confined environments plays a major role in filtration, groundwater flows and a variety of tertiary oil recovery processes. To this end, we study in this section the detailed motion of a tracer particle through an ordered porous environment, by introducing cylindrical obstacles into our system. A

 This journal is © The Royal Society of Chemistry 2013

Published on 17 January 2013 on http://pubs.rsc.org | doi:10.1039/C2SM26727F
Downloaded by Princeton University on 07 February 2013

similar setup has recently been used in microporous flow experiments of micellar solutions.[48–50]

On a microscopic scale, the characteristic features of the confined region are mainly governed by the radius of the cylinders, R, their height, H, the distance between them, D, and their spatial arrangement. In our studies, we chose $H = L_x$ and placed these pillars on a triangular lattice in the flow–vorticity plane. In what follows, we used a simulation box with volume $V = (40 \times 40 \times 140)a^3$ and restricted the confined region to $L_{conf} < L_z$; a schematic representation of our system is provided in Fig. 6. Periodic boundary conditions were applied in the flow as well as in the vorticity direction, and we used the minimum possible periodic cell along the vorticity direction by fixing the pillar spacing to $D = 2R = 0.5L_y$. For such a system geometry, the Reynolds number is then given by:

$$\mathrm{Re} = \frac{2Rv}{\eta/\varrho_s}, \tag{22}$$

where v is the characteristic solvent velocity. In what follows, we will simulate systems at moderate Reynolds numbers with $1 \lesssim \mathrm{Re} \lesssim 35$, since we anticipate a wide variety of possibly nonlinear rheological phenomena in this regime.

From the macroscopic point of view, one of the most relevant quantities to characterize the experiment is the permeability k, which is a measure of the ability of a porous material to allow fluids to pass through it. However, it is a highly non-trivial task to establish a relationship between the aforementioned microscopic quantities and this macroscopic property, since phenomena on very small length-scales, such as eddies and backflows, can have significant ramifications on the overall flow behavior of the fluid. One of the earliest attempts to establish a relationship between the applied pressure gradient $\nabla P \sim g$ and the average *solvent* flux q, *i.e.* the volume of solvent flowing through the unit area in unit time, was made by Darcy in 1856 (ref. 51): he postulated a linear dependence between the two quantities:

$$\nabla P = -\frac{\eta}{k} q. \tag{23}$$

This one-dimensional empirical relationship has frequently served as a starting point for numerous applications and still represents a formidable challenge for theoreticians. More than a century later in 1986, Whitaker developed a rigorous theoretical derivation of Darcy's law for small Reynolds numbers, $\mathrm{Re} \lesssim 1$, by means of volume averaging.[52]

We will be extending our investigations also to higher Reynolds numbers, for which eqn (23) is not *a priori* expected to hold. In order to check the validity of eqn (23) for our system, we recorded the time a tracer particle needs to propagate through the confined region, and defined the flux of *solute* particles through the confinement, $Q \sim q \sim V_z$, as its inverse. We then measured the flux Q of tracer particles with $\sigma = 0.4D$ by sampling the spatial velocity distribution along the gradient direction in steps of $\Delta x = 0.05L_x$ for various g-values. The interaction between the solute particle and the obstacles is modeled akin to U_W [see eqn (5)], and we fixed the position of the solute particle along the x-direction by employing the potential given through eqn (16).

Fig. 7 shows Q as a function of x and g. It is well visible that, similar to the case of an empty channel, the velocity of the tracer particle increases with the distance to the walls and with the magnitude of the pressure gradient. This behavior is however *not* entirely monotonic in the vicinity of the walls: For $g = 0.03$, the flux Q decreases dramatically until it eventually vanishes at $g = 0.035$. Only for $g \geq 0.065$, the tracer particles flow in an unperturbed way.

In order to quantify this highly nonlinear flow behavior, it is instructive to study $\langle Q \rangle$, which represents the flux of solute particles averaged along the gradient direction over the entire channel width. Fig. 8 shows this quantity as a function of g. The broad dispersion of the local velocities for $0.03 \leq g \leq 0.06$ is clearly visible *via* the large error-bars in this range of g.

First, $\langle Q \rangle$ increases linearly with g, confirming thereby the validity of eqn (23) in the regime $1 \lesssim \mathrm{Re} \lesssim 15$, until it starts to drop at $g = 0.03$. From there on, the particle flux is not proportional to the pressure gradient anymore, indicating the absence of laminar flow. Under such flow conditions, Darcy's law is no longer applicable. However, as the acceleration constant eventually exceeds $g = 0.06$, we leave this transient regime and the system enters into a new regime, in which the

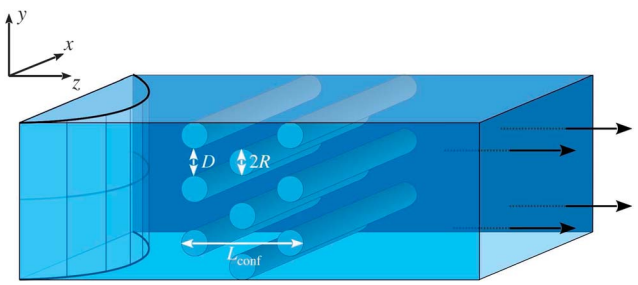

Fig. 6 Schematic representation of the simulation setup. Cylinders with radius R and height L_x are placed in a hexagonal arrangement in the flow–vorticity plane. The spacing between the cylinders is denoted as D. The confined region extends over a length L_{conf} in the flow direction.

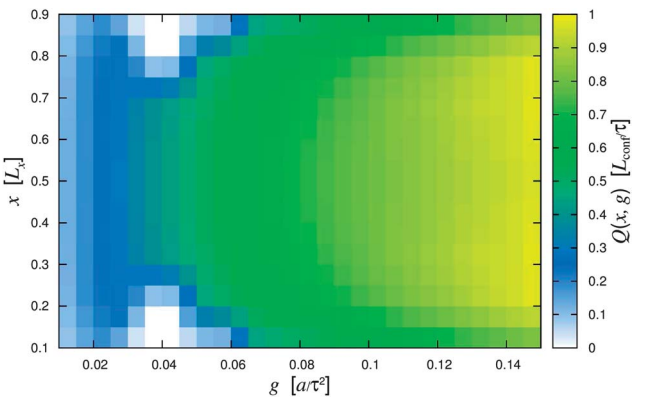

Fig. 7 Color-coded spatial flux Q of particles with $\sigma = 0.4D$ through a confined region with pillar spacing $D = 2R$. Simulations were conducted for a series of acceleration constants g and the solute flux was measured at different positions along the gradient direction.

Published on 17 January 2013 on http://pubs.rsc.org | doi:10.1039/C2SM26727F
Downloaded by Princeton University on 07 February 2013

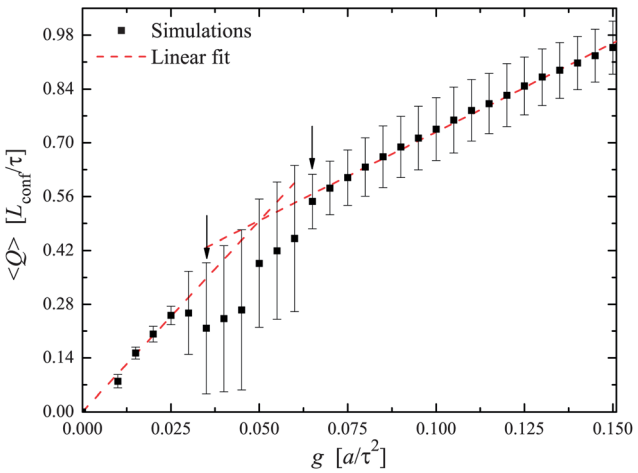

Fig. 8 Average solute flux $\langle Q \rangle$ of a particle propagating through our porous environment as a function of g. Black symbols show results from our MPCD simulations, while the dashed red lines show the corresponding linear fits to our data. The dispersion of the local velocities is reflected in the size of the error-bars. The positions of the vertical arrows are the same as in Fig. 9(a).

dependence on g becomes linear but with a finite offset when extrapolated to $g \rightarrow 0$. We have fitted our data in the unperturbed regions by straight lines, yielding the reduced permeabilities $k_1 = 9.9 \pm 0.3$ and $k_2 = 4.6 \pm 0.1$, respectively. The discrepancy in the k-values points out that we are confronted with two different flow regimes. One might be tempted to interpret the drop of $\langle Q \rangle$ at $g = 0.03$ as the onset of turbulence, but the linear relationship between $\langle Q \rangle$ and g for $g < 0.03$ and for $g > 0.06$ indicates that we have laminar flow in both g-regimes. Such a behavior is definitely not the case for turbulent flow, in which the pressure gradient would have been proportional to the square of the flux.[53]

To be more specific, one has to distinguish with particular caution between two scenarios: (i) the onset of a completely turbulent flow and (ii) the place at which the flow becomes unstable for the very first time. Although in both cases the Reynolds numbers are often referred to as the "critical Reynolds number", the underlying physics of the two scenarios is fundamentally different, since the instability of flow due to small disturbances does not necessarily lead to the emergence of turbulence. In general, a new but still laminar flow profile evolves, which, as the Reynolds number increases further, becomes more unstable and possibly develops into a new laminar flow, but could also undergo a transition into a turbulent flow.

To obtain a clearer picture of the flow behavior in the presence of the obstacles, we also measured the flux of the solvent particles, q, in the absence of any solute particles. The flux was measured immediately after the confined region to capture the effect of the obstacles. The average solvent flux, $\langle q \rangle$, is shown as a function of g in Fig. 9(a); we were able to identify three regimes with distinctly different flow patterns. The inflection points are located at $g = 0.035$ and $g = 0.065$ respectively, and clearly separate the domains. Furthermore, the location of these two points perfectly coincides with the results obtained for the average solute flux, $\langle Q \rangle$, presented in Fig. 8. To demonstrate the dissimilar nature of the regimes, we plotted in Fig. 9(b) the spatial distribution of the solvent flux along the gradient direction for various values of g. For $g \leq 0.03$, the flux has a parabolic shape akin to the case of an empty channel. As g is increased above 0.03, the shape narrows considerably, resembling a Gaussian. Finally, as we enter the domain $g \geq 0.065$, the profile widens again and becomes almost flat in the central region of the channel.

In order to better understand the transient regime at $0.03 \leq g \leq 0.06$, let us consider the two-dimensional flow around a circular obstacle with diameter $2R$. Due to the no-slip boundary conditions on the surface of the obstacle, a boundary layer is created, where the velocity of the solvent changes from a value of zero at the surface to the free flow value some distance away from the cylinder surface. The inertia of the fluid as it rounds the top and bottom of the trailing surface causes the flow to separate at these locations. This creates a perturbed wake downstream from the cylinder. The extent of this perturbation, the so-called *recirculation length* L_r, strongly depends on the obstacle geometry, size and flow strength. In ref. 54

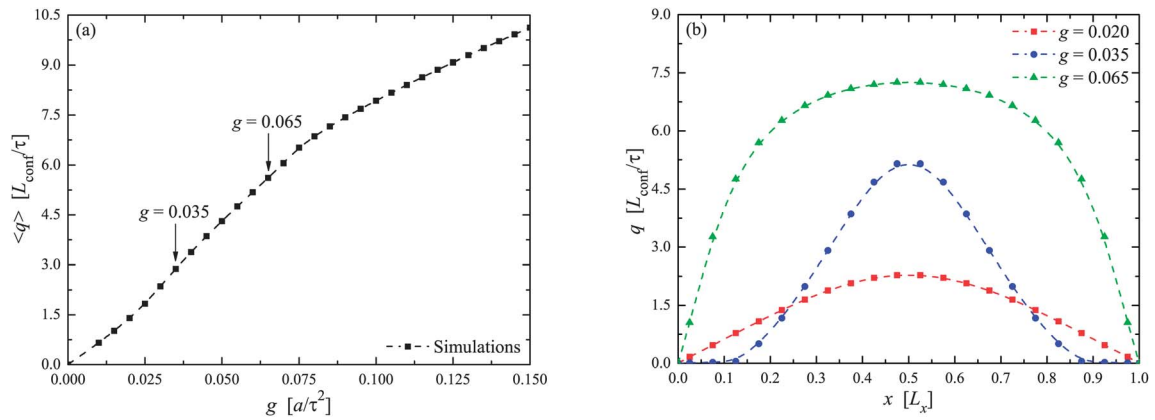

Fig. 9 (a) Average solvent flux $\langle q \rangle$ through the gradient–vorticity plane as a function of g. The vertical arrows indicate the inflection points of the curve at $g = 0.035$ and $g = 0.065$. (b) Spatial distribution of the solvent flux along the gradient direction, $q(x)$, for various values of g. In both cases, the solvent flux was measured immediately after the confined region.

 This journal is © The Royal Society of Chemistry 2013

Published on 17 January 2013 on http://pubs.rsc.org | doi:10.1039/C2SM26727F
Downloaded by Princeton University on 07 February 2013

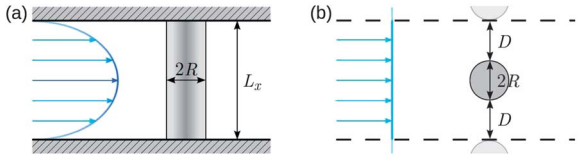

Fig. 10 Pressure driven flow past a single cylindrical obstacle shown in the gradient–flow plane (panel a) and in the vorticity–flow plane (panel b). The hatched gray areas in the left panel represent the impenetrable walls along the gradient direction, while the dashed black lines in the right panel indicates the periodic boundary conditions in the vorticity direction.

(experiments) and ref. 34 (simulations), L_r has been determined for the Poiseuille flow past a *single* cylinder with blocking fractions, defined as $B = 2R/L_y$, up to $B \approx 0.125$. Coutanceau *et al.* established that L_r is a linear function of Re, and that $L_r/2R$ increases with decreasing B (ref. 54). Moreover, Williamson found that the critical Reynolds number, above which the flow becomes unsteady and the Karman vortex street emerges, is approximately Re = 49 (ref. 55).

However, these findings might not be completely applicable to our system, since we have a slightly different setup: in our simulations, the axis of the obstacles is parallel to the gradient direction (see Fig. 6 and 10) and not to the vorticity direction (as in ref. 34 and 54). Thus we do not have Poiseuille flow along the curved surfaces of the cylindrical obstacles, but rather *potential flow*, *i.e.* a flow profile with constant velocity. Furthermore, the blocking fraction $B = 2R/(2D + 2R) = 1/3$ is considerably higher in our simulations.

Therefore we have conducted simulations in which we have evaluated $L_r/2R$ for a single cylinder under potential flow conditions. We also performed additional simulations for Poiseuille flow to quantify the impact of the two different velocity profiles. The results are shown in Fig. 11, where we plotted the relative recirculation length $L_r/2R$ as a function of the Reynolds number Re for the blocking fraction $B = 1/8$ and $B = 1/3$. The errors are estimated to be of the order of $1/(4R)$, since the position of the macroscopic velocities $\boldsymbol{u}_j$ is arbitrarily taken to be the center of the collision cell (see Section II).

First, it is well visible that $L_r/2R$ is proportional to Re and that this quantity increases considerably with decreasing B. Second, we clearly can see that the differences between Poiseuille and potential flow are only marginal for the blocking fractions studied here. This is due to the fact that the curvature of the parabolic profile is essentially flat in the central region. However, we anticipate that the discrepancies between the two flow types will increase for larger B.

With these measurements at our disposal, we can explain the emergence of the transient regime of vanishing flux at $0.03 \leq g \leq 0.06$ (see above). In Fig. 12 we show $L_r/2R$ *vs.* Re, where we indicate the g-values of the disappearance and the re-emergence of stable flow ($g = 0.025$ and $g = 0.065$, respectively) discussed above. From these data it is clearly visible that the origin of the instability is strongly correlated with the recirculation length: when L_r becomes, with increasing Re, comparable to half the gap size, $D/2$, the solvent cannot recover from the perturbation anymore, and thus the flow in the confined region is completely suppressed. Upon further increasing Re, L_r eventually surpasses $D/2$ and the distortion cannot build up anymore, leading to stable laminar flow through the confined section of the channel.

Hence for $\mathrm{Re} \gg 1$, the effects of inertia cannot be neglected anymore, rendering the original form of Darcy's law [eqn (23)] inapplicable. A common extension of this law is the so-called Forchheimer equation,[56,57] which adds an inertial term:

$$\nabla P = -\frac{\eta}{k_1} q - \frac{\varrho_s}{k_2} q^2, \tag{24}$$

introducing the inertial permeability k_2. However, fitting our data to this equation over the entire g-range also failed, due to

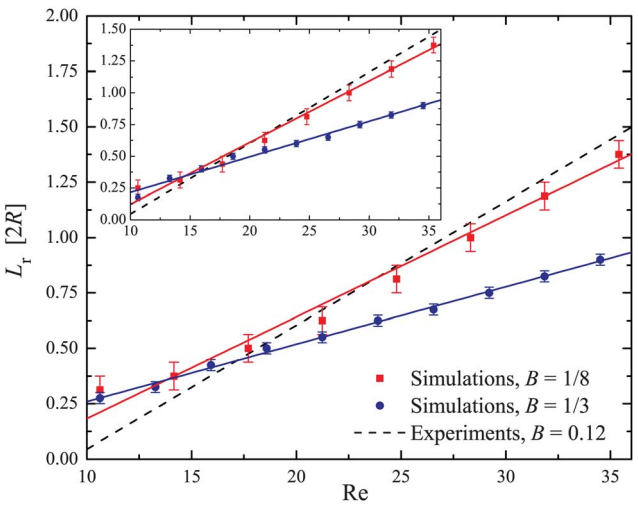

Fig. 11 Relative recirculation length $L_r/2R$ as a function of the Reynolds number Re for blocking fractions $B = 1/8$ and $B = 1/3$. The main panel shows the results under potential flow conditions, while the inset shows the results for Poiseuille flow. Symbols represent simulation data, and the solid lines are linear fits. The dashed black line shows the experimental results for Poiseuille flow past a cylinder from ref. 54.

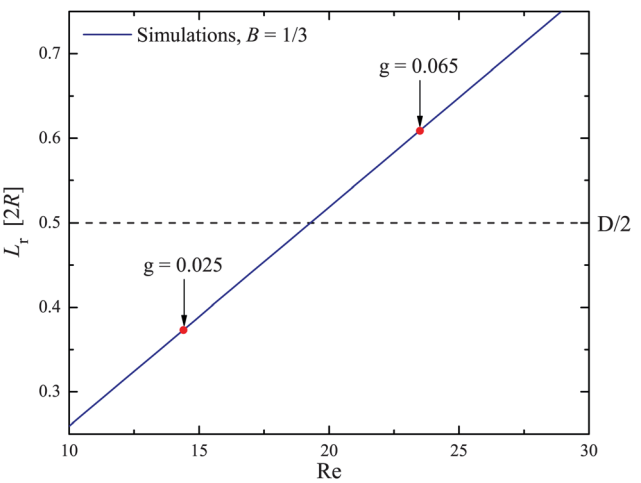

Fig. 12 Relative recirculation length $L_r/2R$ as a function of the Reynolds number Re for a blocking fraction $B = 1/3$. The red symbols mark the disappearance ($g = 0.025$) and the re-emergence ($g = 0.065$) of stable flow in the confined region of the system. The horizontal dashed line indicates $L_r = D/2 = R$.

Published on 17 January 2013 on http://pubs.rsc.org | doi:10.1039/C2SM26727F
Downloaded by Princeton University on 07 February 2013

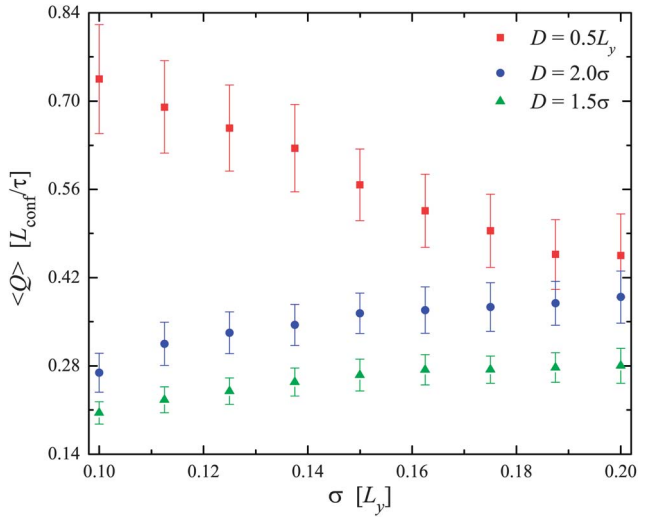

Fig. 13 Particle flux $\langle Q \rangle$ as a function of σ for g = 0.1. Red symbols represent simulation data where we have kept the distance between the cylindrical obstacles fixed at $D = 0.5L_y$. Blue and green symbols show results, where we have kept the *ratio* D/σ fixed at 2.0 and 1.5.

the transient regime in the interval $0.03 \leq g \leq 0.06$ (see Fig. 8), and we can conclude that we are dealing with a non-Darcy flow behavior.

Finally, we studied the influence of the tracer diameter and the size of the obstacles on the solute flux Q. To this end, we have conducted simulations, in which we have (i) varied σ while keeping the gap between the cylindrical obstacles fixed at $D = 2R = 0.5L_y$, and (ii) varied σ while fixing the *ratio* D/σ at 2.0 and 1.5, respectively. The results of these computer experiments are shown in Fig. 13, where we plotted the reduced particle flux $\langle Q \rangle$ relative to the velocity of a non-confined tracer particle of the same size for different values of σ.

(i) For a fixed gap size, $\langle Q \rangle$ decreases with increasing tracer particle size, since the solvent velocity within the gaps is spatially inhomogeneous and shows strong local deviations from a flat profile due to the no-slip boundary conditions at the surface of the cylinders. This scenario is very reminiscent of the propagation of a tracer particle placed in the center of an empty channel (*cf.* Fig. 3).

(ii) The situation is considerably different if we fix the *ratio* between the gap size D and the particle diameter σ, instead. In such a scenario, large particles flow on the average faster through the confinement than small particles. This effect can be understood by considering the radius R of the cylindrical obstacles: in order to keep the ratio D/σ fixed, R has to shrink for bigger solute particles, reducing thereby the surface area of the obstacles and consequently the drag. Hence, the solvent flow is less obstructed and the overall flux increases.

V Conclusions

We have shown that the MPCD technique is capable of reproducing quantitatively experimental results as regards the flow profiles of sizable colloidal particles within narrow channels, even for the extreme cases in which the channel diameter exceeds only slightly the colloidal diameters. Furthermore, simulations have been used to study the effect of geometrically arranged obstacles in a narrow channel, opening the way for further studies of microfluidics in the presence of porous environments; interesting problems include the injection of drilling fluids in rock formations[58] or filtration applications,[59] where the colloidal particles approach the size of the capillary, and classical models for filtration often fail.

Our results can be experimentally verified by means of state-of-the art optical techniques, in which the location and the local velocity of very small tracer particles can be extracted by analysis of the speckle pattern in light scattering experiments.[60] Further studies should address the influence of the geometrical arrangement of the obstacles as well as of the *shape* of the tracer particles on the resulting flow and permeabilities of porous media, as well as the study of flow of colloidal suspensions in finite concentrations.

Acknowledgements

This work has been supported by the Marie Curie ITN-COMPLOIDS (Grant Agreement No. 234810), by the Austrian Science Foundation (FWF) under Proj. No. P19890-N16 and within the SFB ViCoM (Proj.No. F41), and by the Princeton Center for Complex Materials (PCCM), a U.S. National Science Foundation Materials Research Science and Engineering Center (Grant DMR-0819860). Furthermore, A. N. acknowledges a PCCM fellowship.

References

1 W. Pan, D. A. Fedosov, B. Caswell and G. E. Karniadakis, *Microvasc. Res.*, 2011, **82**, 163.
2 R. G. Cox and S. G. Mason, *Annu. Rev. Fluid Mech.*, 1971, **3**, 291.
3 R. G. M. van der Sman, *Soft Matter*, 2009, **5**, 4376.
4 A. Corma, *Chem. Rev.*, 1997, **97**, 2373.
5 G. M. Whitesides and A. D. Stroock, *Phys. Today*, 2001, **54**, 42.
6 T. M. Squires and S. R. Quake, *Rev. Mod. Phys.*, 2005, **77**, 977.
7 D. J. Ehrlich and P. Matsudaira, *Trends Biotechnol.*, 1999, **17**, 315.
8 D. J. Beebe, G. A. Mensing and G. M. Walker, *Annu. Rev. Biomed. Eng.*, 2002, **4**, 261.
9 J. O. Tegenfeldt, C. Prinz, H. Cao, R. L. Huang, R. H. Austin, S. Y. Chou, E. C. Cox and J. C. Sturm, *Anal. Bioanal. Chem.*, 2004, **378**, 1678.
10 L. Bousse, C. Cohen, T. Nikiforov, A. Chow, A. R. Kopf-Sill, R. Dubrow and J. W. Parce, *Annu. Rev. Biophys. Biomol. Struct.*, 2000, **29**, 155.
11 V. Dolnik, S. Liu and S. Jovanovich, *Electrophoresis*, 2000, **21**, 41.
12 G. J. M. Bruin, *Electrophoresis*, 2000, **21**, 3931.
13 L. Zhang, J. M. Koo, L. Jiang, M. Asheghi, K. E. Goodson, J. G. Santiago and T. W. Kenny, *J. Microelectromech. Syst.*, 2002, **11**, 12.
14 R. A. Hayes and B. J. Feenstra, *Nature*, 2003, **425**, 383.

 This journal is © The Royal Society of Chemistry 2013

Published on 17 January 2013 on http://pubs.rsc.org | doi:10.1039/C2SM26727F
Downloaded by Princeton University on 07 February 2013

15 M. E. Staben and R. H. Davis, *Int. J. Multiphase Flow*, 2005, **31**, 529.
16 H. A. Lorentz, *Zittingsverlag Konikl. Akad. Wetensch. Amsterdam*, 1896, **5**, 168.
17 H. Faxén, *Ann. Phys.*, 1922, **373**, 89.
18 P. Ganatos, R. Pfeffer and S. Weinbaum, *J. Fluid Mech.*, 1980, **99**, 739.
19 P. Ganatos, R. Pfeffer and S. Weinbaum, *J. Fluid Mech.*, 1980, **99**, 755.
20 B. H. Yang, J. Wang, D. D. Joseph, H. H. Hu, T.-W. Pan and R. Glowinski, *J. Fluid Mech.*, 2005, **540**, 109.
21 M. E. Staben, A. Z. Zinchenko and R. H. Davis, *Phys. Fluids*, 2003, **15**, 1711.
22 P. K. Ghosh, P. Hänggi, F. Marchesoni, S. Martens, F. Nori, L. Schimansky-Geier and G. Schmid, *Phys. Rev. E: Stat., Nonlinear, Soft Matter Phys.*, 2012, **85**, 011101.
23 L. Ren, W. Qu and D. Li, *Int. J. Heat Mass Transfer*, 2001, **44**, 3125.
24 J. C. Stachowiak, *High Reynolds Number Microfluidic Systems for Drug Delivery*, ed. J. C. Stachowiak, ProQuest, UMI Dissertation Publishing, 2011.
25 B. Li and D. Y. Kwok, *Langmuir*, 2003, **19**, 3041.
26 A. Malevanets and R. Kapral, *J. Chem. Phys.*, 1999, **110**, 8605.
27 G. Gompper, T. Ihle, D. M. Kroll and R. G. Winkler, *Adv. Polym. Sci.*, 2009, **221**, 1.
28 M. Hecht, J. Harting, T. Ihle and H. J. Herrmann, *Phys. Rev. E: Stat., Nonlinear, Soft Matter Phys.*, 2005, **72**, 011408.
29 M. Hecht, J. Harting, M. Bier, J. Reinshagen and H. J. Herrmann, *Phys. Rev. E: Stat., Nonlinear, Soft Matter Phys.*, 2006, **74**, 021403.
30 E. S. Boek, T. F. Headen and J. T. Padding, *Faraday Discuss.*, 2010, **144**, 271.
31 A. Nikoubashman and C. N. Likos, *J. Chem. Phys.*, 2010, **133**, 074901.
32 T. Ihle and D. M. Kroll, *Phys. Rev. E: Stat., Nonlinear, Soft Matter Phys.*, 2001, **63**, 020201.
33 A. Malevanets and R. Kapral, *J. Chem. Phys.*, 2000, **112**, 7260.
34 A. Lamura, G. Gompper, T. Ihle and D. M. Kroll, *Europhys. Lett.*, 2001, **56**, 319.
35 E. Allahyarov and G. Gompper, *Phys. Rev. E: Stat., Nonlinear, Soft Matter Phys.*, 2002, **66**, 036702.
36 J. K. Whitmer and E. Luijten, *J. Phys.: Condens. Matter*, 2010, **22**, 104106.
37 D. A. Lenz, R. Blaak and C. N. Likos, *Soft Matter*, 2009, **5**, 2905.
38 J. T. Padding and A. A. Louis, *Phys. Rev. E: Stat., Nonlinear, Soft Matter Phys.*, 2006, **74**, 031402.
39 A. Malevanets and J. M. Yeomans, *Europhys. Lett.*, 2000, **52**, 231.
40 K. Mussawisade, M. Ripoll, R. G. Winkler and G. Gompper, *J. Chem. Phys.*, 2005, **123**, 144905.
41 M. Ripoll, R. G. Winkler and G. Gompper, *Phys. Rev. Lett.*, 2006, **96**, 188302.
42 C. Tropea, J. F. Foss, and A. Yarin, *Handbook of Experimental Fluid Dynamics*, Springer, 2005.
43 Y. Inoue, Y. Chen and H. Ohashi, *J. Stat. Phys.*, 2002, **107**, 85.
44 J. T. Padding, A. Wysocki, H. Löwen and A. A. Louis, *J. Phys.: Condens. Matter*, 2005, **17**, S3393.
45 H. Brenner and L. J. Gaydos, *J. Colloid Interface Sci.*, 1977, **58**, 312.
46 N. R. Morrow, *Interfacial Phenomena in Petroleum Recovery*, Marcel Dekker Inc., New York, 1991.
47 M. Sahimi, *Rev. Mod. Phys.*, 1993, **65**, 1393.
48 M. Vasudevan, E. Buse, D. Lu, H. Krishna, R. Kalyanaraman, A. Shen, B. Khomani and R. Sureshkumar, *Nat. Mater.*, 2010, **9**, 436.
49 N. Dubash, J. Cardiel, P. Cheung and A. Q. Shen, *Soft Matter*, 2011, **7**, 876.
50 P. Cheung, N. Dubash and A. Q. Shen, *Soft Matter*, 2012, **8**, 2304.
51 H. Darcy, *Les Fontaines Publiques de la Ville de Dijon*, Dalmont, Paris, 1856.
52 S. Whitaker, *Transp. Porous Media*, 1986, **1**, 3.
53 J. H. Spurk, *Fluid Mechanics*, Springer, 1997.
54 M. Coutanceau and R. Bouard, *J. Fluid Mech.*, 1977, **79**, 231.
55 C. H. K. Williamson, *Phys. Fluids*, 1988, **31**, 2742.
56 P. Forchheimer, *Z. Ver. Deutsch. Ing.*, 1901, **45**, 1782.
57 S. Whitaker, *Transp. Porous Media*, 1996, **25**, 27.
58 E. Boek, C. Hall and P. Tardy, *Transp. Porous Media*, 2012, **91**, 479.
59 R. Rajagopalan and C. Tien, *AIChE J.*, 1976, **22**, 523.
60 R. Piazza, private communication, 2012.